FULL RESEARCH ARTICLE

CrossMark

Fused filament fabrication 3D printing with low-melt alloys

Nirupama Warrier[1] · Kunal H. Kate[1]

Abstract

3D-printing polymers using fused filament fabrication (FFF) technology has shown to fabricate complex functional parts for electronic, automotive, and biomedical applications. However, there is limited knowledge and understanding of 3D printing with pure metal feedstock using FFF technology. The use of 3D printing of metals and its alloys using FFF technology can provide low-cost alternatives and solutions to the laser-powder bed fusion process. In current work, low-melting eutectic alloy of bismuth (58% Bi, 42% Sn), non-eutectic alloy of bismuth (40% Bi, 60% Sn), and a non-eutectic alloy of antimony (7.5% Sb, 89% Sn) have been used as a starting material and evaluated for FFF 3D printing using two approaches. In the first approach, a low-melting alloy in the form of wire was used as the feedstock for FFF extrusion. In this approach, the influence of FFF process parameters such as infill ratio, extrusion velocity, feed rate, nozzle temperature and bed temperature on the part fabrication were evaluated for successful fabrication of 2D and 3D geometries and characterized for density, precision, mechanical properties, and microstructure. In the second approach, low-melting alloys were cast onto 3D-printed molds to create metal structures. With this approach, the fabricated specimens were evaluated for its part formability, density, precision, mechanical properties, and microstructure. In addition, both approaches were used to fabricate a prototype specimen such as a souvenir and a prototype wrench. It is expected that such a technology will pave the way for the affordable fabrication of metal prototypes and alternatively on-demand custom metal spare parts for in-space applications and future space missions.

Keywords FFF · FDM · 3D printing · Low-melt alloys · Casting · Metal extrusion

1 Introduction

3D printing can be used to manufacture custom products and has gained a lot of attention due to its flexibility to design complex geometries with metals, polymers, and ceramics [1]. According to the research and advisory board of Gartner Inc., 97.5% of all the 3D printers sold worldwide are Fused filament fabrication (FFF) 3D printers [2]. However, FFF 3D printers are typically limited to 3D print various polymers, whereas metals 3D-printed parts are typically made from 3D-printing technologies such as laser-powder bed fusion (L-PBF), direct metal laser sintering (DMLS), electron beam melting (EBM), and binder jetting. These metal 3D-printing technologies can often take up a lot of space,

are expensive and requires regular maintenance compared to FFF 3D-printing technology [3]. Successful fabrication of metals products using FFF can reduce the price point of metal printers from approximately $500,000 to just $500, paving the way for an affordable desktop metal 3D printer [4]. FFF is an additive manufacturing process in which typically thermoplastic polymers in the form of filaments are fed through an extruder into a heated nozzle, where it is melted and extruded layer-by-layer onto a heated bed platform to fabricate a 3D geometry. Once a layer is fabricated, the nozzle moves up in the z-direction (or, the base is lowered) to accommodate the subsequent layers. This process continues until the desired 3D structure is fabricated [1]. The capability to fabricate metals using FFF technology calls for applications in various fields such as the production of prototypes in industries, disposable single-use surgical instruments in healthcare and manufacturing metal spare parts in the international space station (ISS) and for future space missions such as Mars One.

Recent studies of using FFF technology to print metal use metal infused powder polymer filaments that can be

✉ Kunal H. Kate
kunal.kate@louisville.edu

Nirupama Warrier
ncwarr01@louisville.edu

1 University of Louisville, 2210 S Brook St, 214 Shumaker Research Building, Louisville, KY 40208, USA

fabricated using an FFF 3D printer to form 3D structures. After 3D printing, the polymer content of the fabricated part is removed and the part is sintered, leaving a pure metal object. However, such a process still requires subsequent steps after printing to remove the polymer and get the final metal part [5, 6].

Another approach to use FFF in metal printing is to directly printing with pure metal instead of powder–polymer filament. A study conducted by Hsieh et al. extruded pure metal filaments of low-melting Sn99.3Cu0.7 and Sn60Pb40 alloys in a continuous linear shape with excellent formability [7]. Ten-layer stacking of Sn99.3Cu0.7 and five-layer stacking of Sn60Pb40 was achieved at nozzle temperatures of 220–240 °C. However, attempts to print in 2D was not successful at print separations of less than 0.75 mm. In another study performed by Mireles et al. a redefined extrusion head was used to fabricate 2D spiral maze and a 3D wall with six stacked layers [8]. However, there is not a lot of work in literature that demonstrates successful FFF 3D printing using pure metal as a feedstock to print 3D structures and the mechanical properties that can be achieved with such a process.

In this study, low-melting alloys have been used as feedstock in an FFF 3D printer and evaluated for metal 3D printing. The convenient processing temperatures of low-melting alloys used in this study offer two methods for fabricating metals using a FFF 3D printer. In the first approach, FFF 3D casting, tensile molds were designed and FFF 3D printed in PLA, and low-melt alloys of tin–bismuth and antimony–tin were cast onto the molds to create tensile bar specimens and unique prototype castings. In the second approach, FFF 3D printing, a tin–bismuth alloy in the form of a filament was used as a feedstock for the FFF 3D printer to fabricate tensile specimens. In addition, the FFF 3D cast and FFF 3D-printed samples were characterized for its physical properties, mechanical properties and microstructure. In addition, this work demonstrates the use of FFF technology to fabricate low-melt alloys for applications such as affordable souvenirs and rapid production of metal spare parts for in-space applications.

2 Materials and methods

As a part of studying the feasibility of 3D-printing metals using an FFF 3D printer, a material search was conducted on low-melting alloys through metal reference books, research papers, and commercial websites [9–26]. Due to the temperature limitations of a FFF 3D printer, only low-melting alloy systems with onset melting temperatures ranging from of 100–300 °C were considered. In addition, the lead content was limited to a maximum composition of 10%. The materials screened included 21 eutectic alloys systems of bismuth, indium, and tin, and 55 non-eutectic alloy systems of bismuth, indium, tin, antimony, cadmium, silver and lead [9–26].

2.1 Materials for FFF casting and printing

Using the above pre-screening, a low-melting eutectic alloy of bismuth (58% Bi, 42% Sn), non-eutectic alloy of bismuth (40% Bi, 60% Sn), and a non-eutectic alloy of antimony (7.5% Sb, 89% Sn) were selected for the study on the basis of their physical and mechanical properties. Sn42Bi58, also known by its trade name 'Cerrotru', and Sn60Bi40 are shiny in appearance and exhibits low viscosity values, making them good candidates for casting application [10]. The typical applications of the bismuth–tin alloy include lead-free soldering, metal spraying, proof casting, prototyping, and radiation shielding [11]. Sn89Sb7.5, commonly known as 'Babbitt' is white and shiny in appearance, soft, readily conformable and hence easily cast. The material also exhibits excellent corrosion resistance properties and resilience under a wide range of conditions. It is widely used as a bearing material [12]. Table 1 shows the physical and mechanical properties of Sn42Bi58, Sn60Bi40 and Sn89Sb7.5. All three materials in Table 1 were used to fabricate and test 3D tensile bars with the method-I called FFF 3D casting, whereas Sn60Bi40 alloy was used to FFF fabricate and test 3D tensile bars with method II called FFF 3D printing.

2.2 Method-I: FFF 3D casting

For FFF 3D casting the mold of the specimens to be cast was designed in SolidWorks, and 3D printed using an FFF 3D printer. The top and isometric views of the tensile molds designed for fabrication is shown in Fig. 1.

The model was saved in '.STL' format and imported into the 3D-printing software, Repetier. The mold was 3D printed using an FFF 3D Printer, Printrbot simple 1403, in polylactic acid (PLA) material. Printing process parameters included nozzle temperature of 215 °C, bed temperature of 65 °C and infill percentage of 40%. Infill percentage was lowered to aid the easy removal of the part from the mold with minimum damage.

Table 1 Physical and mechanical properties of the low-melting alloys selected for the evaluation of metal fabrication using FFF [26–29]

Specimen	MP (°C)	Density (g/cc)	UTS (MPa)	Elongation (%)
Sn42Bi58	138	8.58	55.41	46
Sn60Bi40	138–170	8.21	62.5	35
Sn89Sb7.5	241–354	7.38	90	10

Fig. 1 SolidWorks design of the tensile specimen mold. **a** Top view, **b** isometric view
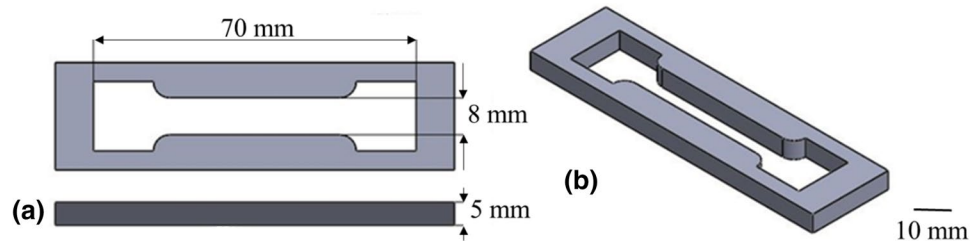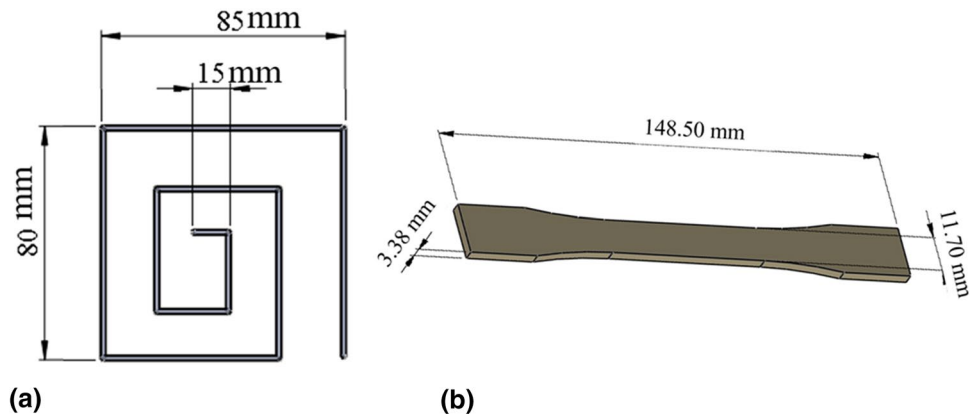

Fig. 2 SolidWorks designs for the development of printing process parameters of low-melting alloy, Sn60Bi40, using FFF 3D-printing technology; **a** 2D-square maze toolpath; **b** 3D-dog bone specimen

The low-melt alloys were heated to its approximate pouring temperatures of 280 °C (Sn60Bi40, Sn42Bi58) and 450 °C (Sn89Sb7.5) using a hotplate. The molten alloy was then cast into the 3D-printed tensile molds and cooled to room temperatures. In addition, to investigate the effect of mold cooling times on the mechanical properties and microstructure of the fabricated part, additional specimens of Sn60Bi40 were cast at different cooling rates. The cast was cooled in two different states viz. slow cooled, at room temperature (cooling time = 15 s) and fast cooled under the presence of an external fan (cooling time = 5 s). This methodology was used to create four ASTM E8 standard tensile specimens. The specimens were subsequently characterized for its dimensions, and physical properties such as mass, volume, and density, mechanical properties such as ultimate tensile strength, yield strength, and percent elongation as well as the microstructure.

2.3 Method II: FFF 3D printing

For FFF 3D printing, an important aspect of getting quality prints is its ability to continuously deposit material and adhere it onto the print bed to form a 2D or 3D geometry. A 2D geometry, square maze toolpath, was designed to investigate the linear deposition characteristics of Sn60Bi40. Multiple trials were performed to achieve continuous deposition. This was followed by attempts to fabricate a 3D geometry, dog bone specimen. Printrbot Simple 1403 with a build volume of 6″ × 6″ × 6″ was used for the fabrications. Figure 2 shows the SolidWorks models of the 2D tool path, and the
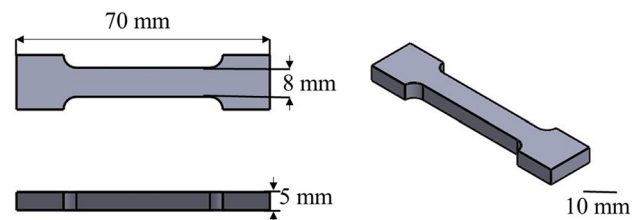

Fig. 3 SolidWorks design of the ASTM E8 standard tensile specimen for FFF 3D printing with Sn60Bi40 alloy

dog bone specimen used for the development of process parameters.

Once the FFF-printing process parameters for fabricating low-melt Sn60Bi40 was successfully developed. ASTM E8 standard tensile coupons were fabricated using the parameters as per the dimensions, as shown in Fig. 3. The specimens were subsequently tested for its physical properties such as mass, volume, and density, mechanical properties such as ultimate tensile strength, yield strength, and percent elongation as well as the microstructure.

3 Characterization

Samples fabricated using both methods I and II were further post-processed. ALO papers with grits P120, and P240, were used as the abrasive surface and the specimen was polished on a water lubricated abrasive wheel. The dimensions and mass of the samples were noted. The volume and density

were calculated based on Archimedes' principle, with the liquid of submersion being water. Tensile testing was performed using a uniaxial MTI 10,000 lbs benchtop tension-testing machine. From tensile testing, stress–strain curves were plotted to compute materials properties such as ultimate tensile strength, percent elongation, and yield strength.

The fabricated specimens were then carefully sectioned using a metal pressed diamond-wafering blade to a convenient size along its *z*-axis. After sectioning, the sample was mounted in an epoxy compression mounting resin material to facilitate handling during the subsequent grinding and polishing steps. The sample was then ground and polished using P240, P400 and P1200 grit ALO papers [30]. Further fine polishing was performed on the abrasive surface of 0.25 μm with a speed of 100 rpm to prepare a smooth surface for etching out the microstructure. Polishing was performed for a duration of 1800s at a rate of 100 rpm and a force of approximately 10 pounds [31]. Lastly, after polishing the Sn60Bi40 and Sn42Bi58 alloys were etched using 95% methanol, 3% HCl and 2% HNO_3 to reveal the true microstructure. The Sn89Sb7.5 alloy was subjected to chemical etching with a 5% solution of HCl in ethanol.

4 Results and discussion

4.1 FFF 3D casting

The process for FFF 3D casting and the ASTM E8 tensile specimens fabricated using this technique are shown in Fig. 4.

4.1.1 FFF 3D casting of Sn60Bi40, Sn42Bi58 and Sn89Sb7.5 alloys

The dimensions of the post-processed specimens were evaluated to understand the geometric tolerances of the fabricated part.

Table 2 shows the dimensions and tolerances of the post-processed FFF 3D cast parts of Sn60Bi40, Sn42Bi58 and Sn89Sb7.5 alloys.

Table 2 Dimensions of the post-processed FFF 3D cast parts of Sn60Bi40, Sn42Bi58 and Sn89Sb7.5 alloys

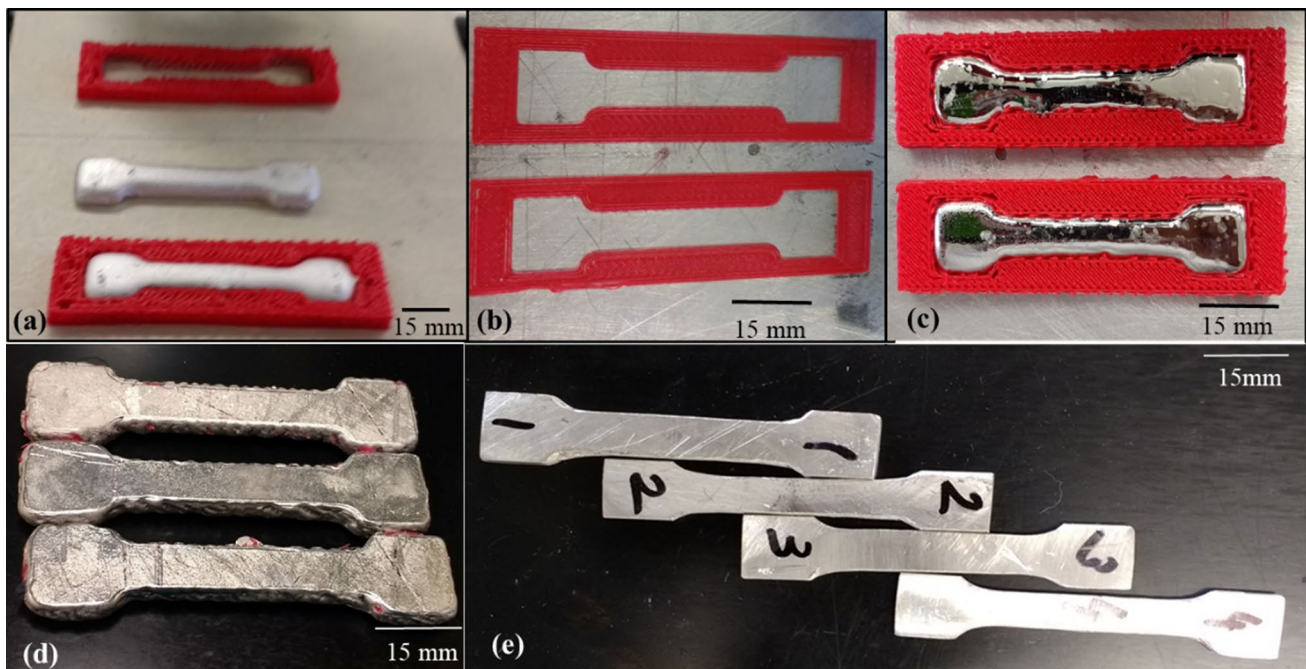| Specimen	Length (mm)	Width (mm)	Thickness (mm)
Sn60Bi40	69.36 ± 20	7.97 ± 0.23	4.73 ± 0.31
Sn42Bi58	69.10 ± 0.44	8.14 ± 0.12	4.64 ± 0.49
Sn89Sb7.5	68.81 ± 0.39	8.32 ± 0.2	5.55 ± 0.37

Fig. 4 **a** Process summary of the FFF cast methodology, **b** tensile molds 3D printed using PLA, **c** molten material cast onto the 3D-printed mold, **d** as-cast tensile specimens, **e** post-processed tensile specimens

Table 2 shows that the average length of the fabricated samples is a bit smaller than the true length of 70 mm, with an average dimension of 69.9 ± 0.34 mm. The width of the samples was found to vary in ranges of 7.97–8.32 mm, with an average value of 8.15 ± 0.21 mm. The thickness of the samples was found to lie between values of 4.64–5.55 mm with an average value of 4.98 ± 0.39 mm. The greatest variation in dimensions was found to occur in the width of the specimen, with a percentage error of 1.80%. The least variation in dimension occurred in the thickness of the specimen, with a percentage difference value of 0.48%. The length measurements had a percentage error value of 1.31%.

Table 3 shows the physical properties of the post-processed FFF 3D cast parts of Sn60Bi40, Sn42Bi58 and Sn89Sb7.5 alloys. Table 3 shows that the average volume of the fabricated specimens in comparison to the expected volume derived from SolidWorks (3.762 g/cc), is 19.22%. The greatest percent error in volume was for the parts fabricated in Sn42Bi58, with a percentage error of 24.53%. Parts fabricated in Sn89Sb7.5 and Sn60Bi40 exhibited percentage differences of 17.2 and 15.93%, respectively. Consequently, the mass of the fabricated specimens was found to greatly vary for the parts fabricated in Sn42Bi58, with a percentage error of 24.36%. Parts fabricated in Sn89Sb7.5 and Sn60Bi40 exhibited percentage differences of 17.74 and 14.74%, respectively.

The densities of the fabricated specimens are in close correlation with the true density values of the materials and accounted to relative densities of 98.15% for the Sn60Bi40, 100% for the Sn42Bi58 and 97.15% for Sn89Sb7.5. Figure 5 shows the relative density of the post-processed FFF 3D cast parts of Sn60Bi40, Sn42Bi58 and Sn89Sb7.5 alloys. Figure 5 shows that the densities of the post-processed FFF 3D cast parts of Sn60Bi40, Sn42Bi58 and Sn89Sb7.5 alloys are in close correlation with the true density values of the alloys, as shown in Table 1.

Figure 6 shows the ultimate tensile strength of the post-processed FFF 3D cast parts for Sn60Bi40, Sn42Bi58 and Sn89Sb7.5 alloys. The ultimate tensile strength (UTS) of the post-processed FFF 3D cast parts of Sn60Bi40, Sn42Bi58 and Sn89Sb7.5 alloys are 60.29 ± 2.79, 55.08 ± 0.58 and 94.81 ± 16 MPa, respectively. This is a percentage increase of 3.53 and 0.60% for Sn60Bi40 and Sn42Bi58, respectively, with respect to the estimated values of the UTS, as given

in Table 1. UTS value of Sn89Sb7.5 shows a percentage decrease of 5.34% as with respect to the expected values, which could be due to the high geometric tolerances and lower relative densities of the fabricated part, as depicted in Table 2 and Fig. 5, respectively.

The percentage elongation of the post-processed FFF 3D cast parts of Sn60Bi40, Sn42Bi58 and Sn89Sb7.5 alloys are 30.18 ± 0.99, 34.22 ± 3.43 and $15.38 \pm 4.10\%$, respectively. It can be noted that Sn42Bi58 has higher percentage elongation compared to that of Sn60Bi40. This can be attributed to higher percentage composition of bismuth in the alloy. At higher concentrations of bismuth, a greater number of bismuth particles are non-soluble and thus precipitated and accumulated at the grain boundaries, leading to a decrease in the overall stiffness of the material [32]. Sn89Sb7.5 has low values of percentage elongations and is hence comparatively brittle.

Figure 7 shows percent elongation of the post-processed FFF 3D cast parts of Sn60Bi40, Sn42Bi58 and Sn89Sb7.5 alloys.

Figure 8 shows yield strengths of the post-processed FFF 3D cast parts of Sn60Bi40, Sn42Bi58 and Sn89Sb7.5 alloys. The yield stress of the samples was calculated using the 0.2% offset method [33]. The yield stress of the post-processed
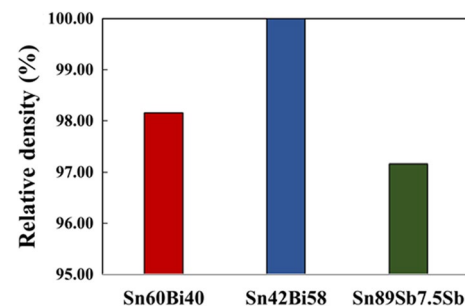

Fig. 5 Relative densities of the post-processed FFF 3D cast parts of Sn60Bi40, Sn42Bi58 and Sn89Sb7.5 alloys
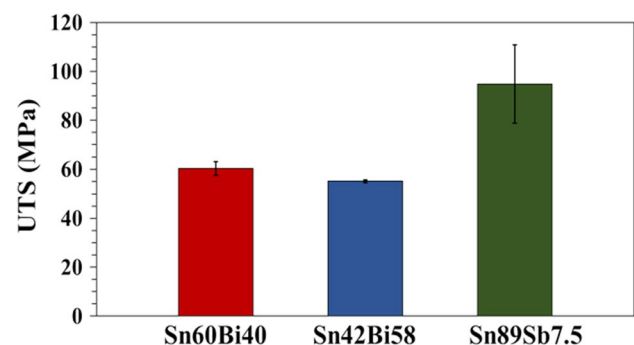

Fig. 6 Ultimate tensile strength of the post-processed FFF 3D cast parts of Sn60Bi40, Sn42Bi58 and Sn89Sb7.5 alloys
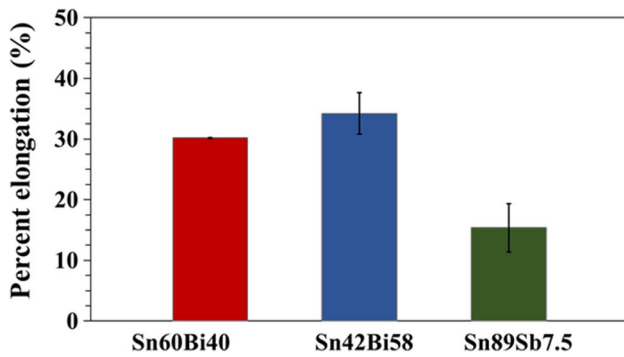
Table 3 Physical properties of the post-processed FFF 3D cast parts of Sn60Bi40, Sn42Bi58 and Sn89Sb7.5 alloys

Specimen	Mass (g)	Volume (cc)	Density (g/cc)
Sn60Bi40	25.57 ± 1.385	3.207 ± 0.180	7.97 ± 0.206
Sn42Bi58	25.27 ± 2.538	2.94 ± 0.289	8.58 ± 0.027
Sn89Sb7.5	32.18 ± 2.54	4.47 ± 0.251	7.17 ± 0.243

Fig. 7 Percent elongation of the post-processed FFF 3D cast parts of Sn60Bi40, Sn42Bi58 and Sn89Sb7.5 alloys
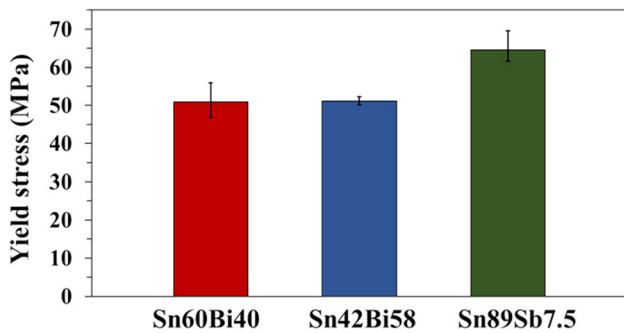

Fig. 8 Yield strengths of the post-processed FFF 3D cast parts of Sn60Bi40, Sn42Bi58 and Sn89Sb7.5 alloys

FFF 3D cast parts of Sn60Bi40, Sn42Bi58 and Sn89Sb7.5 alloys are 50.90 ± 4.32, 51.19 ± 1.12 and 64.54 ± 7.35 MPa, respectively.

The optical microscopy images of the post-processed FFF 3D cast parts of Sn42Bi58, and Sn60Bi40 alloy is shown in Fig. 9. Figure 9a, c shows that microstructure of a bismuth–tin alloy consists of bismuth-rich phases, tin-rich phases and fine granules of bismuth precipitates in the tin-rich phase [34].

The dark grey pattern in the bright field images represent the bismuth-rich phase, the light grey background represents the tin-rich phase, and the fine dark particles on the tin-rich matrix represent the bismuth precipitates. The precipitation of bismuth occurs due to the lower solubility of bismuth in the tin at low temperatures, leading to the segregation of bismuth from the tin [35]. As the concentration of bismuth content in the alloy increases from 40% in Sn60Bi40 to 58% in Sn42Bi58, bismuth particles segregate significantly and accumulate on the tin-rich phase [36].

Figure 9b, d shows the corresponding dark field images, clearly distinguishes the lamellar structure of the eutectic and non-eutectic bismuth–tin alloys. It can be observed that in the eutectic alloy (Sn42Bi58), the bismuth phase, as well as the tin phase, forms a continuous network in the form of

a dendrite, also referred to as the fishbone eutectics. The microstructure of the non-eutectic alloy (Sn60Bi40) consists of a continuous network of bismuth surrounded by the tin-rich matrix [32]. Figure 10 shows the optical microscopy images of the post-processed FFF 3D cast parts of the Sn89Sb7.5 alloy.

Figure 10 shows that the microstructure of the Sn89Sb7.5 alloy consists of Sn–Sb phase surrounded by Sn-rich phase and Cu–Sn phase. Sn–Sb phases are square in shape, and the Cu–Sn phases are the long and irregular shaped phases in the background of the Sn-rich phase (Fig. 10) [37, 38].

4.1.2 Effect of cooling rate on the FFF 3D casting of Sn60Bi40 alloy

The dimensions of the post-processed specimens were evaluated to understand the geometric tolerances of the fabricated part. Table 4 shows the dimensions and tolerances of the post-processed FFF 3D cast parts of Sn60Bi40 at slow and fast rates of cooling.

Table 4 shows that the length of the fabricated samples is smaller than the true length of 70 mm, with an average dimension of 68.88 ± 0.47 mm and a percentage error of 1.61%. The fabricated samples had an average width of 7.78 ± 0.29 mm and a percentage error of 2.77%. The greatest variation in dimensions was found to occur in the thickness of the specimen, with an average thickness of 5.11 ± 0.44 mm and percentage error value of 2.08%. Table 5 shows the physical properties of the post-processed FFF 3D cast parts of Sn60Bi40 at slow and fast rates of cooling.

Table 5 shows that the volume of the fabricated specimens is smaller than the expected volume derived from the SolidWorks, 3.762 g/cc, by a percentage of 11.31%. The parts fabricated in slowly cooled condition under ambient temperature exhibited percentage differences of 9.23% and the percent volume error percent for the fast-cooled specimen was 13.39%. Consequently, the mass of the specimens fabricated in the slow and fast-cooling conditions exhibited percentage error values of 9.27 and 8.99%, respectively.

The densities of the fabricated specimens are found to be in close correlation with the true density value of the Sn60Bi40 alloys, as shown in Table 1. Figure 11 shows the relative density of the post-processed FFF 3D cast parts of Sn60Bi40 at slow and fast rates of cooling, which account for percentage differences of 99.63% for the slowly cooled specimens and 99.77% for the fast-cooled specimens.

Figure 11 shows that the densities of the post-processed FFF 3D cast parts of Sn60Bi40 at slow and rapid rates of cooling is in close correlation with the true density value of the Sn60Bi40 alloy, as shown in Table 1. Figure 12 shows ultimate tensile strengths of the post-processed FFF 3D cast parts of Sn60Bi40 at slow and fast rates of cooling.
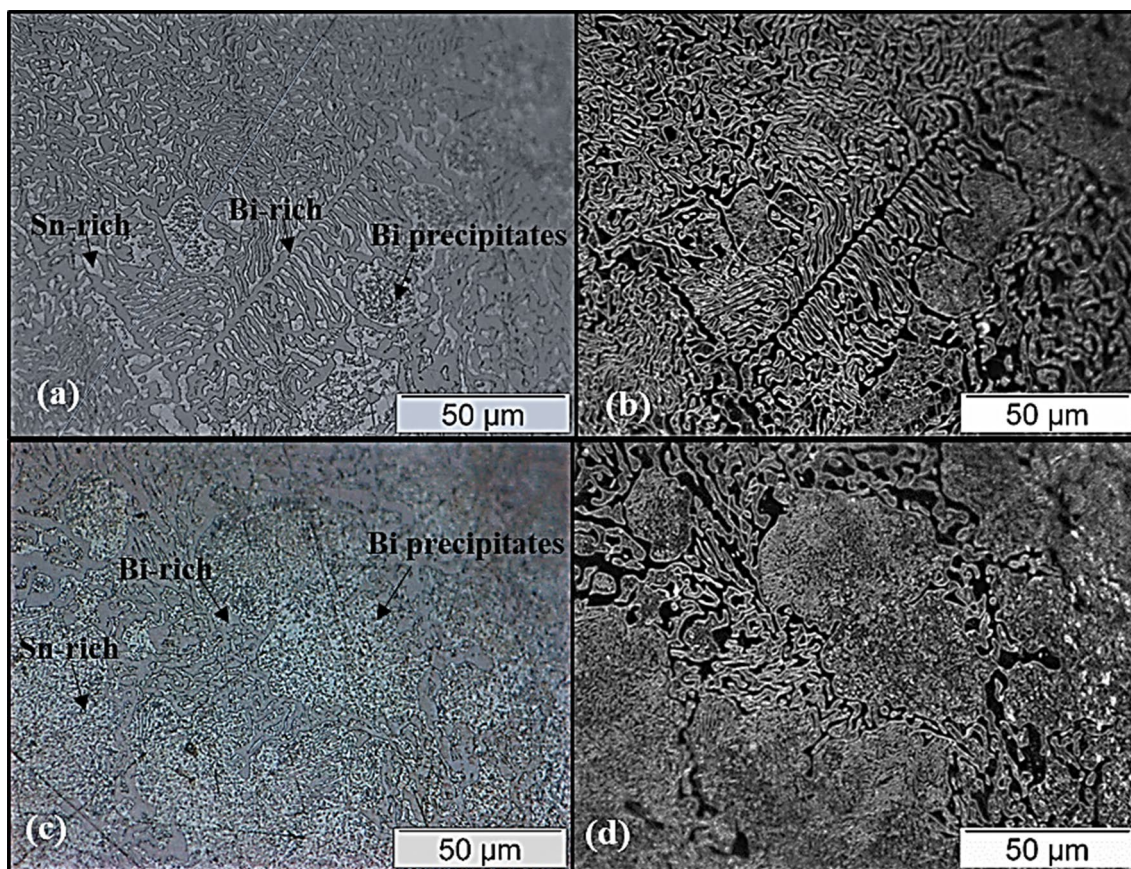
Fig. 9 Optical microscopy images of the post-processed FFF 3D cast Sn42Bi58 (eutectic) and Sn60Bi40 (non-eutectic) alloys. **a** Bright field image of Sn42Bi58 showing bismuth and tin phases in the microstructure. **b** Dark field image of Sn42Bi58 showing the eutectic structure. **c** Bright field image of Sn60Bi40 showing bismuth and tin phases in the microstructure. **d** Dark field image of Sn60Bi40 which shows the primary Sn-rich phase surrounded by eutectic structure
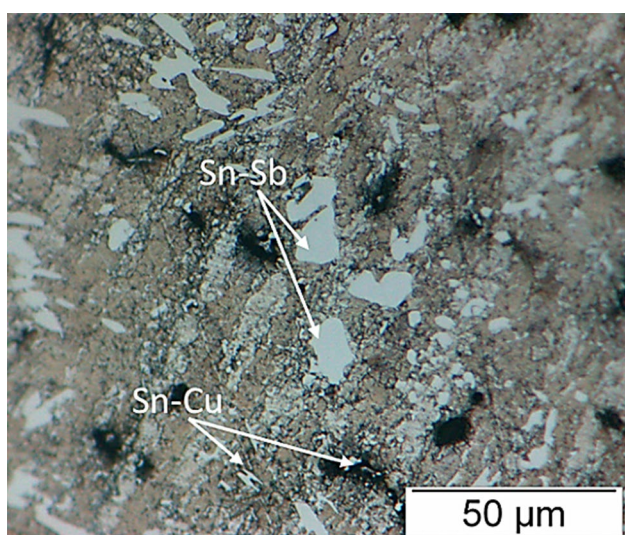

Fig. 10 Optical microscopy image of the post-processed FFF 3D cast part of the Sn89Sb7.5 alloy

Table 4 Dimensions and tolerances of the post-processed FFF 3D cast parts of Sn60Bi40 at slow and fast rates of cooling

Rate of cooling	Length (mm)	Width (mm)	Thickness (mm)
Slow cooled	68.79 ± 0.22	7.56 ± 0.22	5.23 ± 0.63
Fast cooled	68.98 ± 0.72	8.01 ± 0.37	4.98 ± 0.25

Table 5 Physical properties of the post-processed FFF 3D cast parts of Sn60Bi40 at slow and fast rates of cooling

Rate of cooling	Mass (g)	Volume (cc)	Density (g/cc)
Slow cooled	27.84 ± 2.52	3.43 ± 0.161	8.09 ± 0.009
Fast cooled	27.92 ± 2.34	3.29 ± 1.56	8.10 ± 0.057

Figure 12 represents the average ultimate tensile strength of the post-processed FFF 3D cast parts of Sn60Bi40 at slow and fast rates of cooling which are 73.35 ± 3.69 and 92.10 ± 0.58 MPa, respectively. This is a percentage increase of 15.97% for the slow-cooled specimen and 47.36% for the
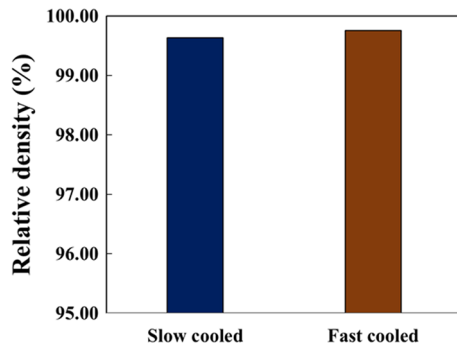
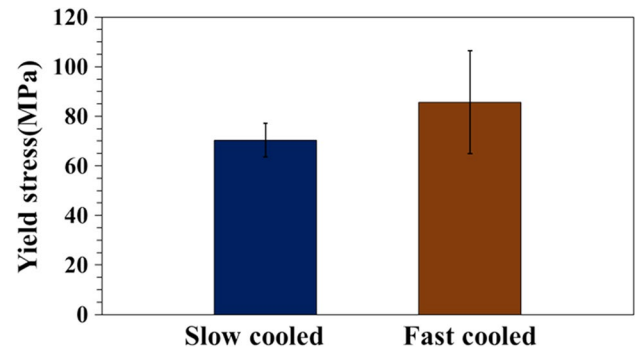Fig. 11 Relative densities of the post-processed FFF 3D cast parts of Sn60Bi40 at slow and fast rates of cooling
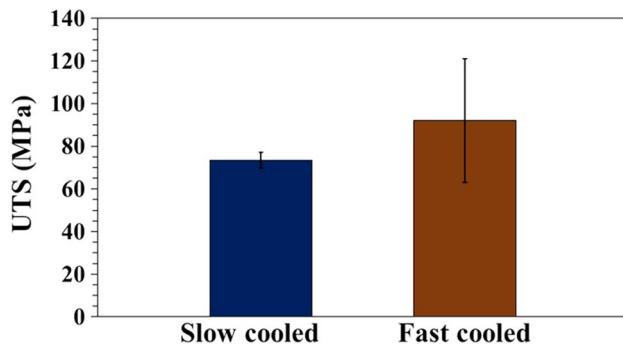

Fig. 12 Ultimate tensile strengths of the post-processed FFF 3D cast parts of Sn60Bi40 at slow and fast rates of cooling
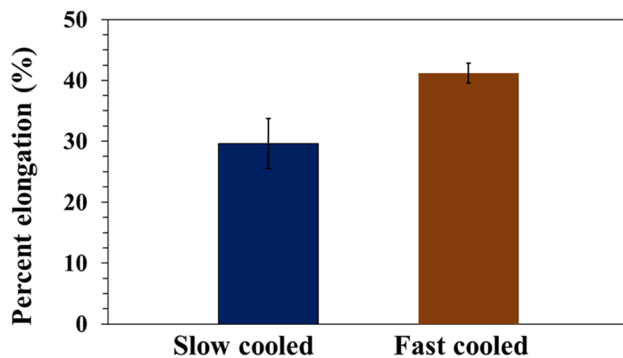

Fig. 13 Percentage elongation of the post-processed FFF 3D cast parts of Sn60Bi40 at slow and fast rates of cooling

fast-cooled specimen with respect to the estimated values of the UTS for the Sn60Bi40 alloy, as shown in Table 1. Fast-cooled specimens exhibit higher ultimate tensile strengths.

Figure 13 shows percentage elongation values of the post-processed FFF 3D cast parts of Sn60Bi40 at slow and fast rates of cooling.

Percentage elongation of the post-processed FFF 3D cast parts of Sn60Bi40 at slow and fast rates of cooling are

Fig. 14 Yield strengths of the post-processed FFF 3D cast parts of Sn60Bi40 at slow and fast rates of cooling

29.62 ± 4.11 and $41.17 \pm 1.64\%$, respectively. Fast-cooled specimens clearly exhibit higher percentage elongation, with an increase of 17.61% as compared to the estimated value (see Table 1), and hence higher ductility.

Figure 14 shows yield strength of the post-processed FFF 3D cast parts of Sn60Bi40 at slow and fast rates of cooling.

The yield stress of the FFF 3D cast samples was calculated using the 0.2% offset method [35]. The yield stresses of the slow-cooled and fast-cooled specimens of Sn60Bi40 are 70.37 ± 6.70 and 87.68 ± 20.46 MPa, respectively. Fast-cooled samples exhibit higher yield strength.

The optical microscopy images of post-processed FFF 3D cast parts of Sn60Bi40 at slow and fast rates of cooling is shown in Fig. 15.

Figure 15 shows that the microstructure of the slowly cooled specimen consists of a continuous network of bismuth and tin phase in the form of a lamellar structure surrounded by tin-rich phase containing Bi precipitates. As the rate of cooling is increased, the microstructure forms closed colonies with finer grain structures and closer grain boundaries, as shown in Fig. 15b. This leads to ductility enhancement and explains the higher values of percentage elongation of the fast-cooled specimens, as shown in Fig. 13 [37].

4.2 FFF 3D printing of Sn60Bi40 alloy

The printing parameters such as the velocity of extrusion, the rate of feeding, the temperature of the nozzle, the print-bed temperature and the layer height play a significant role in the continuous deposition of the material, adherence to the bed (and subsequent layers) and build quality of the fabricated part. The parameters were iterated experimentally to successfully 3D print Sn60Bi40 alloy using the FFF technology.

DSC/TGA analysis was conducted on the Sn60Bi40 alloy to study the melting characteristics, and the nozzle temperature was iterated at increments of 5 °C to identify 220 °C as the ideal temperature for extrusion. The bed temperature
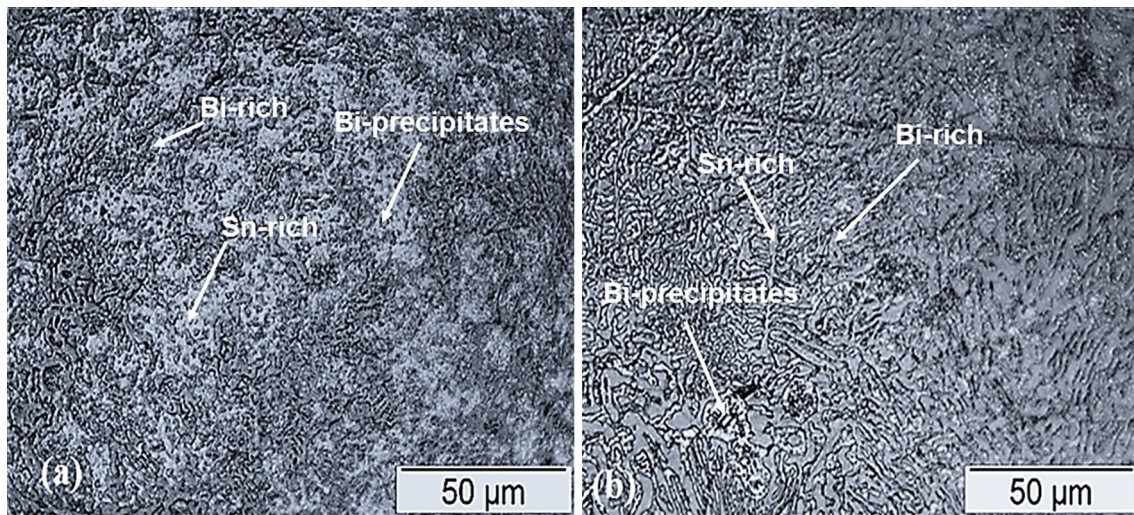
Fig. 15 a Optical microscopy image of the slow-cooled non-eutectic Sn60Bi40 material, **b** optical microscopy image of the fast-cooled non-eutectic Sn60Bi40 material showing closer colonies

was set to 40 °C for better adherence to the print-bed and faster cooling of the metal alloy. The infill percentage was set at 80% and the layer height was set to 0.3 mm for optimal deposition of the printed layers.

Multiple trials were conducted to achieve a continuous deposition of the Sn60Bi40 alloy in 2Dimensions. Initial trials of fabricating the 2D geometry at extrusion velocities of 14 mm/s and feed rate of 150 mm/s deposited discontinuous tracks with a gap of approximately 7 mm between extrusions, as shown in Fig. 16a. Reducing the extrusion velocities to 7 mm/s provided additional time for depositing the material on to the print bed. Consequently, increasing the feed rate to a higher value of 200 mm/s assisted in the faster extrusion of the material. Thus, the coupled effect of

reducing the extrusion velocity by 50% and increasing the feed rate by 25% resulted in successful fabrication of the Sn60Bi40 alloy in 2D, as shown in Fig. 16b. The perimeter of the 2D square tool path spans a total length of 320 mm.

Attempts to fabricate the 3D geometry using the parameters developed for 2D created irregular intervals of separations, as shown in Fig. 17a probably due to the lack of molten material available for immediate extrusion. Increasing the feed rate by a percentage of 20% along with a decrease in 28.57% in the extrusion velocity addressed this issue reducing the discontinuities over the entire area of the geometry, as shown in Fig. 17b. Reducing the extrusion velocity further to an allowed minimum of 1 mm/s further reduced the voids and discontinuities between the layers and paved the
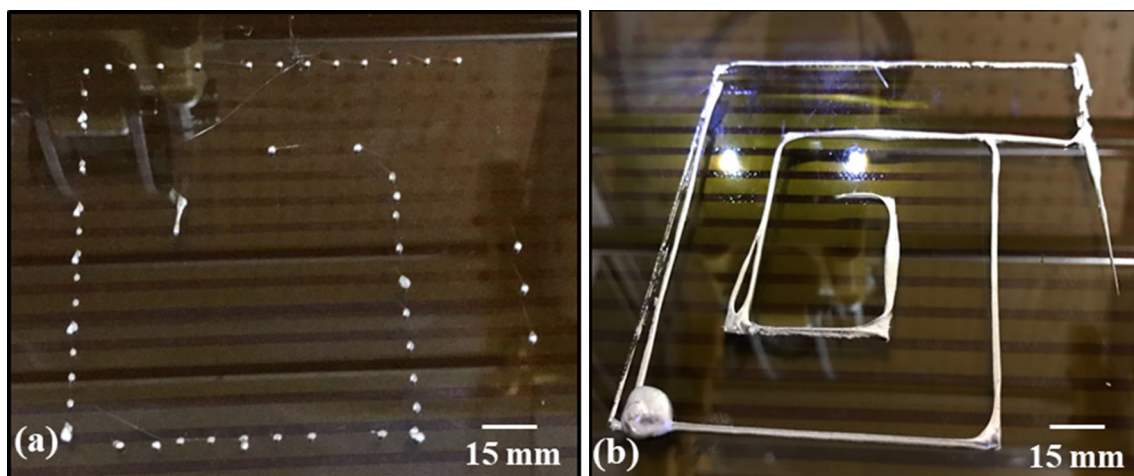

Fig. 16 a Trial 1—2D square maze toolpath with discontinuity between depositions, **b** Trial 2—successful fabrication of 2D square maze toolpath
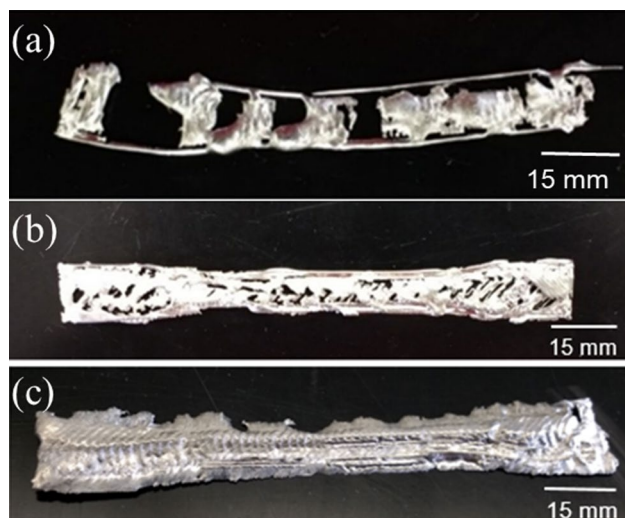
Fig. 17 FFF 3D printing of 3D geometry using Sn60Bi40 alloy, **a** Trial 1, **b** Trial 2, **c** Trial 3

Table 6 Printing process parameters developed for fabricating low-melting Sn60Bi40 alloy using FFF 3D-printing technology

Printing parameters	2D		3D		
	Trial 1	Trial 2	Trial 1	Trial 2	Trial 3
Nozzle temperature (°C)	220	220	220	220	220
Bed temperature (°C)	40	40	40	40	40
Extrusion velocity (mm/s)	14	7	7	5	1
Feed rate (mm/s)	150	200	200	250	250
Layer height (mm)	0.3	0.3	0.3	0.3	0.3
Infill (%)	NA	NA	80	80	80

Fig. 18 FFF 3D-printed ASTM E8 standard tensile specimen of Sn60Bi40 alloy

way for the successful fabrication of Sn60Bi40 using FFF technology, as shown in Fig. 17c. The structure exhibits nearly complete fill with sufficient interlayer bonding.

Table 6 shows the process parameters that were developed for the fabrication of 2D and 3D geometries of the Sn60Bi40 alloy using the FFF 3D-printing technology.

Finally, ASTM E8 standard tensile specimens were fabricated as per the print parameters developed, as given in table (3D, Trial 3) and shown in Fig. 18.

Table 7 shows the dimensions and physical properties of the post-processed FFF 3D-printed part of the Sn60Bi40 alloy.

Table 7 shows that the length of the fabricated samples is smaller than the true length of 70 mm, with an average dimension of 69.19 ± 0.69 mm and a percentage error of 1.16%. The fabricated samples had an average width of 7.99 ± 0.35 mm and percentage error value of 0.13%. The greatest variation in dimensions was found to occur in the thickness of the specimen, with an average thickness of 4.88 ± 0.15 mm and percentage error values of 2.43%. The volume of the fabricated specimens is lesser than the expected volume derived from the SolidWorks, 3.762 g/cc, by a percentage of 31.08%. Consequently, the mass of fabricated specimens had a percentage error of 35.63%. The average densities of the fabricated specimens are 93.91% and lower than the true density of the material. The ultimate tensile strength, yield strength and percent elongation of the FFF 3D-printed ASTM E8 tensile specimen of Sn60Bi40 is shown in Fig. 19.

The ultimate tensile strength of the FFF 3D-printed tensile specimen is 41.55 ± 2.30 MPa. This is a percentage decrease of 33.52% with respect to the estimated values of the UTS of the Sn60Bi40 alloy (see Table 1). Similarly, the percent elongation of the FFF 3D-printed tensile specimen is 16.38 ± 1.59 MPa. This is a percentage decrease of 53.21% with respect to the estimated values of the percent elongation of the Sn60Bi40 alloy (see Table 1). This could be due to the lower volume percentages and lower relative densities of the fabricated part, as depicted in Table 7. The yield stress of the samples was calculated using the 0.2% offset method and is 34.06 ± 3.43 MPa [37]. The optical microscopy images of post-processed FFF 3D-printed part of Sn60Bi40 alloy is shown in Fig. 20.

Figure 20a shows that microstructure of the FFF 3D-printed Sn60Bi40 alloy consists of bismuth-rich phases, tin-rich phases and fine granules of bismuth precipitates in the tin-rich phase [39]. The light grey pattern in Fig. 20a represent the bismuth-rich phase; the dark grey background represents the tin-rich phase and the fine light-colored particles on the tin-rich matrix represent the bismuth precipitates. The
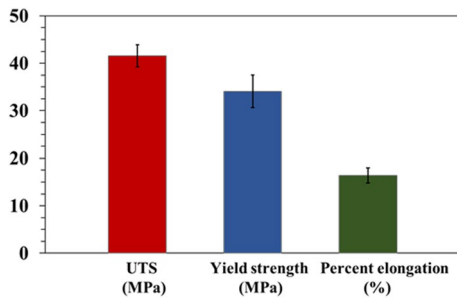
Table 7 Dimensions and physical properties of the post-processed FFF 3D-printed part of the Sn60Bi40 alloy

Length (mm)	Width (mm)	Thickness (mm)	Mass (g)	Volume (cc)	Density (g/cc)
69.19 ± 0.69	7.99 ± 0.35	4.88 ± 0.15	21.31 ± 2.05	2.75 ± 0.25	7.71 ± 0.11

Fig. 19 Ultimate tensile strength, yield strength and percent elongation of the FFF 3D-printed ASTM E8 tensile specimen of Sn60Bi40

precipitation of bismuth occurs due to the lower solubility of bismuth in the tin at low temperatures, leading to the segregation of bismuth from the tin. At a magnification of 20×, layering of fine and coarse microstructure was observed, as shown in Fig. 20b. The coarsening of the lamellar could be attributed to the reheating of the previous build layer by the subsequent layer [8].

The FFF 3D-printed parts exhibited low relative densities of 93.91% and low mechanical properties of ultimate tensile strength, yield strength and percent elongation, as shown in Fig. 19. This is reflected in the microstructure of the alloy (Fig. 20) and can be attributed to the reheating of the previous build layer by the subsequent layer. The FFF 3D Cast specimens exhibited comparable dimensional accuracy, densities and mechanical properties. Relative densities are in close correlation with the true density values of the materials and are equal to 98.15% for the Sn60Bi40 alloy, 100% for the Sn42Bi58 alloy and 97.15% for Sn89Sb7.5 alloy. The fast-cooled specimen

of Sn60Bi40 exhibited an enhanced relative density of 99.77%, an ultimate tensile strength of 147.36% and percentage elongation of 117%.

5 Applications

The capability of fabricating metals using an FFF 3D printing highlights the potential of fabricating unique prototypes and low-volume parts with minimal cost and lead times, in the fields of automobile, aerospace, tooling, healthcare and consumer industries. The International Space Station houses a 3D printer; however, it is limited to fabricating parts only in thermoplastic material, and not in metals [40]. Using the FFF 3D-printing methodology, the prototype of a mechanical spanner was 3D printed in Sn60Bi40 alloy. Figure 21a shows the prototype of mechanical spanner 3D printed using FFF 3D-printing technology. Using the FFF 3D casting methodology, a customized souvenir of UofL (University of Louisville) logo was fabricated. Figure 21b shows the customized UofL souvenir fabricated using the FFF 3D casting methodology.

FFF casting exhibits higher dimensional accuracy, 100% relative density and 99.4% UTS for the eutectic Sn–Bi material and can thus be used to cast a similar wrench design or any other tooling equipment in space application for on-demand and custom 3D printing. Other possibilities include the fabrication of customizable single-use disposable surgical instruments in healthcare, which can be customized according to the patient's physique, and rapid production of customized jewelry.
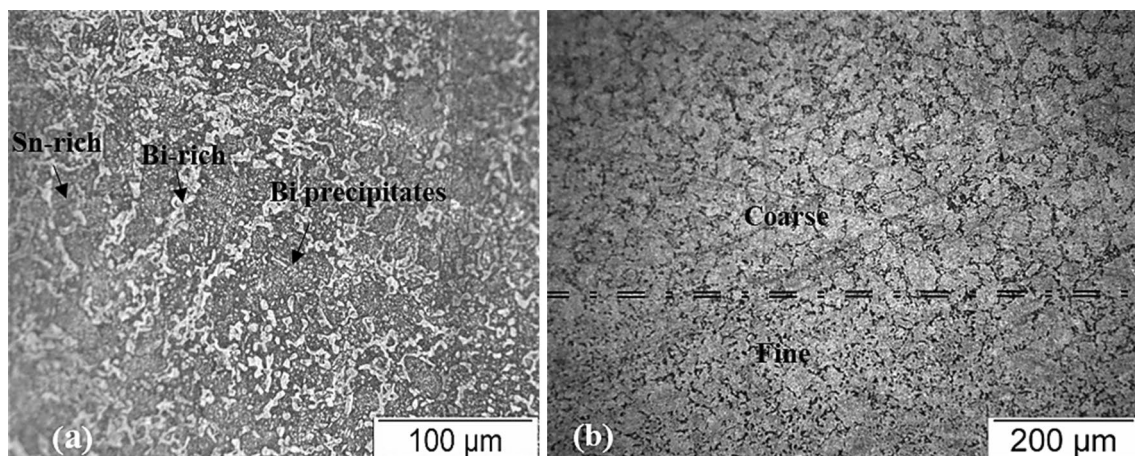

Fig. 20 a Bright field (BF) image of FFF 3D-printed Sn60Bi40 alloy showing the primary tin-rich phase surrounded by eutectic structure (×50). **b** Dark field (DF) image of FFF 3D-printed Sn60Bi40 alloy which shows the layering of fine and coarse microstructure
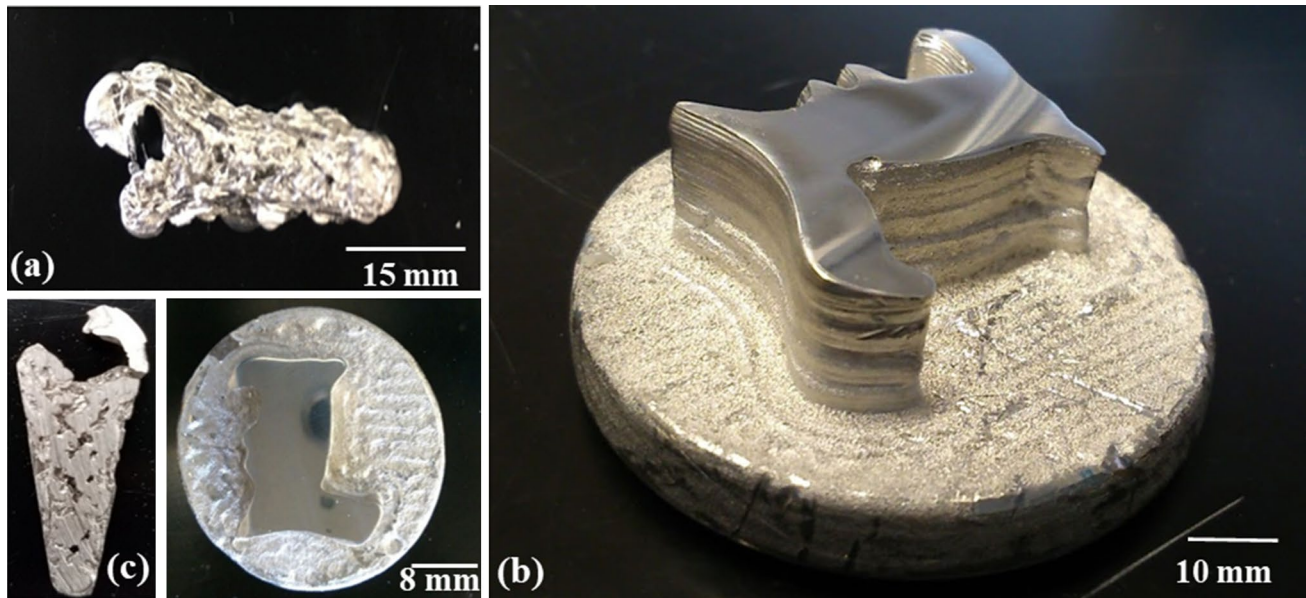
Fig. 21 Metal prototypes fabricated using an FFF 3D printer. **a, c** Mechanical wrench fabricated using FFF 3D-printing methodology. **b, d** Customized UofL (University of Louisville) souvenir logo fabricated using FFF 3D casting methodology (**c**)

6 Conclusion

The research conducted showcases the feasibility of fabricating low-melting metals using the FFF 3D printing technology using either the FFF casting or printing with pure metal filaments as feedstock. The FFF printing provides lower relative densities of 93.91% that result in relative lower mechanical properties compared to FFF casting that gave near full density parts. This indicates that further optimization of the FFF 3D printing process parameters requires coupling the effects of feed rate and extrusion velocity and formulating a correlation between the frequency of extrusion, speed of extrusion and the print velocity. This could improve the geometric tolerances of the FFF 3D-printed parts and improve the mechanical properties of the product. For the FFF 3D cast technology, material properties such as the pouring temperature and the cooling rate determine the dimensional tolerances and the quality of the part 3D printed. Fast-cooled specimens exhibit enhanced densities and mechanical properties in comparison to the slow-cooled specimens. This work paves the potentiality of FFF in the rapid production of affordable metal prototypes and fully functional parts in industries, and on-demand 3D printing of metals in space.

References

1. Gibson I, Rosen D, Stucker B (2014) Additive manufacturing technologies: 3D printing, rapid prototyping, and direct digital manufacturing. Springer, Berlin
2. Grunewald SJ, Gartner Inc. 3D printer sales are expected to double in 2016, reach 5.6 million units sold by 2019. https://3dprint.com/98653/3d-printer-sales-double-2016/. Accessed 13 Sept 2017
3. Wong KV, Hernandez A (2012) A review of additive manufacturing. ISRN Mech Eng. https://doi.org/10.5402/2012/208760
4. Sculpteo. FDM vs SLS 3D Printing – What They Mean and When To Use Them. https://www.sculpteo.com/en/3d-printing/fdm-vs-sls-3d-printing-technologies/. Accessed 13 Sept 2017
5. Fafenrot S, Grimmelsmann N, Wortmann M, Ehrmann A (2017) Three-dimensional (3D) printing of polymer-metal hybrid materials by fused deposition modeling. Materials 10(10):1199. https://doi.org/10.3390/ma10101199
6. Gonzalez-Gutierez J, Godec D, Gur NR, Spoerk M, Kukla C, Holzer C (2018) 3D printing conditions determination for feedstock used in fused filament fabrication (FFF) of 17-4ph stainless steel parts. Metabk 57(1–2):117–120
7. Hsieh P, Tsai C, Liu B, Wei W, Wang A, Luo R (2016) 3D printing of low melting temperature alloys by fused deposition modeling. In: Industrial Technology (ICIT), (2016) IEEE international conference 2016, IEEE, pp 1138–1142
8. Mireles J, Kim H-C, Lee IH, Espalin D, Medina F, MacDonald E, Wicker R (2013) Development of a fused deposition modeling system for low melting temperature metal alloys. J Electron Packag 135(1):011008
9. CSU (2007) Composition and physical properties of alloys. http://www5.csudh.edu/oliver/chemdata/alloys.htm. Accessed 13 Sept 2017
10. 5NPLUS (2012), Product data sheet MCP 137/Metspec 281 alloy. https://www.5nplus.com/files/10/Alloy%20137%20Tech%20Data%20Sheet_2016-07-22-15-34.pdf. Accessed 10 Nov 2017

11. 5NPLUS (2012) Product data sheet MCP 150/ Metspec 281/338 alloy. https://www.5nplus.com/files/10/Alloy%20150%20Tech%20Data%20Sheet_2016-07-22-15-35.pdf. Accessed 10 Nov 2017

12. Belmont (2017) Material Data Sheet 7881 Genuine Babbitt. http://www.belmontmetals.com/wp-content/uploads/2017/09/L-1015-B.pdf. Accessed 10 Nov 2017

13. Bolotoff P (2010) Solder alloys: physical and mechanical properties. Alasir Enterprises. http://alasir.com/reference/solder_alloys/ . Accessed 10 Nov 2017

14. Briggs E (2011) Advantages of bismuth-based alloys for low temperature Pb-free soldering and rework. In: International conference on soldering and reliability, surface mount technology association (SMTA), Toronto

15. EPI Metals Catalog (2017) EPI, indium/specialty alloys. http://www.espimetals.com/. Accessed 13 Sept 2017

16. Indium Corporation (2017) Product data sheet, eutectic gold tin solder. http://www.indium.com/. Accessed 13 Sept 2017

17. Cverna F (2002) ASM ready reference: Thermal properties of metals. ASM International, Materials Park, Ohio

18. Kaap Alloys and Wires Inc (2017) Kapp cadmium–zinc multipurpose solders. http://www.kappalloy.com/cad-zinc-solder.php. Accessed 10 Nov 2017

19. Lee N-C (1997) Getting ready for lead-free solders. Solder Surf Mt Technol 9(2):65–69

20. Materia T The world's most comprehensive materials database. https://www.totalmateria.com/. Accessed 13 Sept 2017

21. Meilunas M, Primavera A, Dunford SO (2002) Reliability and failure analysis of lead-free solder joints. In: Proceedings, IPC conference

22. Metals B. Low melting (fusible) alloys. http://www.belmontmetals.com/product-category/low-melting-fusible-alloys/. Accessed 10 May 2018

23. Sheet PD (1997) Solder wire. Indium Corporation of America, Utica

24. Smith DR, Siewert TA, Stephen L, Madeni JC (2002) Database for solder properties with emphasis on new lead-free solders, NIST and Colorado School of Mines. E Release 4:1–77

25. Smithells CJ (1967) Metals reference book, vol 1. Butterworth, Oxford

26. Thompson J (1930) Properties of lead–bismuth, lead–tin, type metal and fusible alloys, Bureau of Standards Journal of Research. National Bureau of Standards 5(5):1085–1107

27. Bauccio M (1993) ASM metals reference book. ASM International, Materials Park, Ohio

28. Solder D Qualitek, technical datasheet-Sn42/Bi58 solid solder wire. https://www.qualitek.com/sn42bi58solderwiretechdata.pdf. Accessed 6 May 2018

29. Belmont Casting alloys for rubber molds (RM-1097). https://belmont.com. Accessed 10 May 2018

30. Metallurgical sample preparation microscopy and SEM sample preparation. https://www.labtesting.com/services/materials-testing/metallurgical-testing/sample-preparation. Accessed 10 Nov 2017

31. Tin alloy specimen preparation. http://www.metallographic.com/Procedures/Tin%20alloys.htm. Accessed 10 Nov 2017

32. Shen L, Wu Y, Wang S, Chen Z (2017) Creep behavior of Sn–Bi solder alloys at elevated temperatures studied by nanoindentation. J Mater Sci Mater Electron 28(5):4114–4124

33. Beer FP, Johnston R, Dewolf J, Mazurek D (2006) Mechanics of materials. McGraw-Hill, Boston

34. Mei Z, Morris JW (1992) Characterization of eutectic Sn–Bi solder joints. J Electron Mater 21(6):599–607. https://doi.org/10.1007/bf02655427

35. Lai Z, Ye D (2016) Microstructure and fracture behavior of non eutectic Sn–Bi solder alloys. J Mater Sci Mater Electron 27(4):3182–3192. https://doi.org/10.1007/s10854-015-4143-4

36. Spinelli J (2015) Microstructural development and mechanical properties of a near-eutectic directionally solidified Sn–Bi solder alloy. Mater Char 107:43–53

37. Leszczynska-Madej B, Madej M (2013) Effect of the heat treatment on the microstructure and properties of tin babbitt. Kovove Mater Metall Mater 51(2):101–110

38. Korobov YS, Nevezhin SV, Filippov MA, Ilyushin VV, Potekhin BA, Gogolev LV (2012) Effect of production methods on tribological characteristics of babbitt coatings. J Frict Wear 33(3):190–194. https://doi.org/10.3103/s1068366612030063

39. Morris JW, Goldstein JLF, Mei Z (1993) Microstructure and mechanical properties of Sn–In and Sn–Bi solders. JOM 45(7):25–27. https://doi.org/10.1007/bf03222376

40. NASA (2014) Space station 3-D printer builds ratchet wrench to complete First Phase Of Operations. https://www.nasa.gov. Accessed 10 Nov 2017